

# Nanoscale Mapping of Hydrogen Evolution on Metallic and Semiconducting MoS<sub>2</sub> Nanosheets

Tong Sun,<sup>1#</sup> Hanyu Zhang,<sup>2#</sup> Xiang Wang,<sup>1</sup> Jun Liu,<sup>2</sup> Chuanxiao Xiao,<sup>2</sup> Sanjini U. Nanayakkara,<sup>2</sup>  
Jeffrey L. Blackburn,<sup>2</sup> Michael V. Mirkin,<sup>1\*</sup> and Elisa M. Miller<sup>2\*</sup>

<sup>1</sup>Department of Chemistry and Biochemistry, Queens College–CUNY, Flushing, NY 11367 and  
Graduate Center of CUNY, New York, NY 10016, United States

<sup>2</sup>Materials and Chemical Science and Technology Directorate, National Renewable Energy  
Laboratory, Golden, CO 80401, United States

#authors contributed equally to the work

\*corresponding authors: Michael.Mirkin@qc.cuny.edu and Elisa.Miller@nrel.gov

Hydrogen evolution reaction (HER) on molybdenum disulfide (MoS<sub>2</sub>) nanosheets is enhanced for the metallic (1T) phase relative to the thermodynamically stable semiconducting (2H) phase. To measure this difference, we employ scanning electrochemical microscopy (SECM) for high-resolution mapping (<20 nm spatial resolution) of surface reactivity for mixed-phase and pure 2H-only MoS<sub>2</sub> nanosheets. For mixed-phase MoS<sub>2</sub> nanosheets, we find major differences in reactivity of the two phases for electron transfer involving ferrocenemethanol, allowing us to locate 1T and 2H regions and directly map the corresponding HER activity. In our measurements, we find that HER is immeasurably slow on the 2H basal plane and much faster on edges, whereas 1T portions are highly reactive across the entire MoS<sub>2</sub> nanosheet. We also use scanning transmission electron microscopy-electron energy loss spectroscopy and scanning

Kelvin probe microscopy to corroborate the phase domains and local workfunctions (surface potentials) within the MoS<sub>2</sub> nanosheets; the mixed-phase MoS<sub>2</sub> has a lower workfunction compared to 2H MoS<sub>2</sub>, which could enable a greater driving force for H<sub>2</sub> generation. This powerful combination of techniques for spatially mapping surface reactivity and correlated phase domains should be applicable to a broad range of materials for HER and other catalysis reactions.

Dihydrogen ( $H_2$ ) is a carbon-free fuel with high volumetric energy density that can be readily transported.<sup>1</sup> An attractive method for generating carbon-neutral  $H_2$  is *via* catalytic water splitting, and thus far expensive platinum-based catalysts are the most efficient for the hydrogen evolution reaction (HER).<sup>2</sup> Alternative materials, such as transition metal dichalcogenides, have been investigated for HER, where molybdenum disulfide ( $MoS_2$ ) has attracted a lot of attention.<sup>3-8</sup> In order for  $MoS_2$  to compete with Pt, its catalytic activity for HER must be improved. Strategies towards this goal include doping, creating defect sites, exposing more edge sites by quantum confinement, straining, and phase engineering.<sup>9-19</sup>

By quantum confining  $MoS_2$  and reducing it to the 1T phase from the thermodynamically stable (2H) phase, several groups obtained promising HER results.<sup>5, 9, 15, 16, 18, 20</sup> Researchers have shown very high HER activity at 2H  $MoS_2$  edges and within 1T  $MoS_2$ , prompting the creation and study of morphologies with enhanced surface area and edge sites for 2H and a large portion of the 1T phase.<sup>19-22</sup> Since the 1T phase is thermodynamically unstable, it reverts back to the 2H phase with time, and ongoing efforts are aimed at slowing or eliminating this 1T-to-2H conversion process.<sup>13, 15, 20, 23, 24</sup> However, as the 1T phase reverts to the 2H phase, there is still significant uncertainty surrounding the catalytic contributions of isolated sheets of pure phase (1T *or* 2H) and various sites (edge, interior grain boundaries) within nanosheets having mixed-phase (2H *and* 1T). In such a dynamically evolving nanoscale system, a number of questions remain to be addressed that require simultaneous nanoscale resolution of morphology, electronic structure, and catalytic activity. Such questions include: How and where (spatially) does the conversion from 1T to 2H occur, and how can it be controlled? How do interior sites, edge sites, and domain boundaries evolve spatially in time, both in terms of phase and catalytic activity?

Understanding such factors can provide important mechanistic insights into the kinetics and thermodynamics of HER on complex nanostructured catalysts.

In this communication, we use scanning electrochemical microscopy (SECM) to spatially probe the 1T and 2H domains within a nanosheet and how this leads to differences in HER activity and heterogeneous electron transfer rate throughout the nanosheet. SECM,<sup>25,26</sup> scanning ion conductance microscopy,<sup>27</sup> scanning electrochemical cell microscopy (SECCM),<sup>28-31</sup> and scanning tunneling microscopy<sup>32</sup> have previously been used to obtain nanoscale maps of catalytic activity; however, these types of studies on 2D MoS<sub>2</sub> have been limited. Li et al. demonstrated with SECM that strained vacancies within 2D MoS<sub>2</sub> led to higher HER activity.<sup>33</sup> The HER activity has not been measured with high-spatial resolution across *mixed-phase* MoS<sub>2</sub> nanosheets, directly showing the changes in activity at the edges, interior sites, and 2H/1T boundary. In SECM, the reactivity of electrocatalysts is characterized by scanning a small tip electrode above the catalyst's surface to measure local reactant and product fluxes and determine the local rates of specific heterogeneous reactions.<sup>25, 26, 34-39</sup> Here we use well-characterized, polished nanodisk tips<sup>35, 37, 39</sup> to map catalytic HER activity of mixed-phase MoS<sub>2</sub> nanosheets with < 20 nm lateral resolution. We pair the SECM probe with scanning transmission electron microscopy-electron energy loss spectroscopy (STEM-EELS) and scanning Kelvin probe microscopy (SKPM) to further characterize the 1T and 2H phase domains. Our results on mixed-phase MoS<sub>2</sub> nanosheets indicate that the 1T phase tends to be surrounded by the 2H phase. Also, the edges of 2H MoS<sub>2</sub> are active for HER while the interior sites have little to no activity; the HER activity is most prevalent within the 1T MoS<sub>2</sub> and is essentially constant from edge to center.

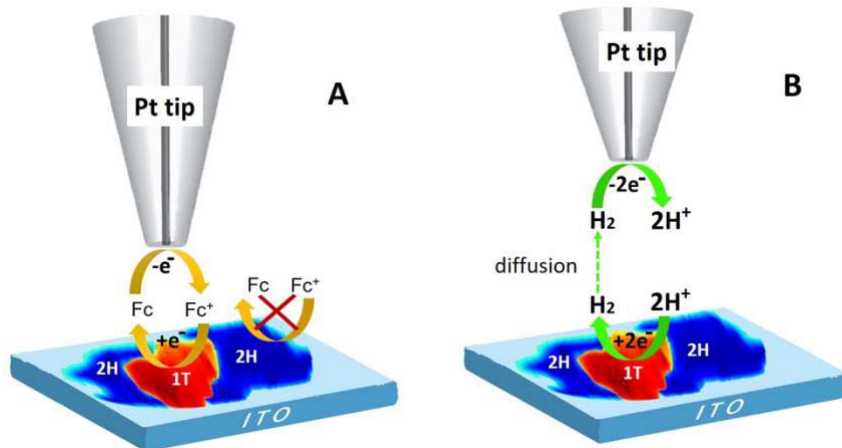


**Figure 1.** Schematic illustrating mechanism of SECM image contrast of MoS<sub>2</sub> nanosheets. Schematic representation of (A) positive feedback produced by oxidation/reduction of Fc and (B) probing HER at the MoS<sub>2</sub> surface in the SG/TC mode. Not to scale.

We employ the feedback mode of SECM (Figure 1A), with ferrocenemethanol (Fc) mediator to locate the 1T and 2H regions on the surface of MoS<sub>2</sub> nanosheets and then map the corresponding reactivity toward HER using substrate generation/tip collection (SG/TC) mode (Figure 1B; see SI for detailed SECM discussion). Three experimental current vs. distance ( $i_T$  vs.  $d$ ) curves obtained over the ITO surface and over 2H and mixed-phase MoS<sub>2</sub> nanosheets are shown in Figure S1A. The  $i_T - d$  curves obtained with the Fc mediator show major differences in electron-transfer reactivities, which result in the negative feedback at 2H MoS<sub>2</sub> (curve 1), low positive feedback over ITO (curve 2), and significantly higher positive feedback at the 1T MoS<sub>2</sub> surface (curve 3). These differences, which stem from high surface conductivity of metallic 1T MoS<sub>2</sub> and low conductivity of the semiconductive 2H phase, are used to identify the phases in MoS<sub>2</sub> nanosheets. A 2D color map of two 2H MoS<sub>2</sub> nanosheets (Figure S1B) on ITO shows uniformly negative feedback current over 2H MoS<sub>2</sub> and small positive feedback current over ITO.

The synthesis of 2H MoS<sub>2</sub> nanosheets is detailed in the SI. Briefly, we deposit the solution-exfoliated (predominantly 1T) nanosheets onto indium-doped tin oxide (ITO) substrates and thermally anneal the nanosheets in N<sub>2</sub> to fully convert them to 2H. A micrometer-scale SG/TC mode image (Figure 2A) shows significant HER activity for the edge of a 2H flake. The feedback mode image obtained with the Fc mediator and a smaller tip ( $a = 18$  nm) shows higher resolution on the edge of a flake (Figure 2B). The hydrogen evolution activity of the same area is mapped with the same tip in SG/TC mode (Figure 2C), and the high-resolution map clearly demonstrates that the HER activity is confined to the flake edge, whose reactive width appears to be <50 nm. The true width of the reactive edge may be significantly narrower than that in Figure 2C due to the diffusional broadening effect, which is observed for any redox species generated at the substrate and is characteristic of this technique.<sup>25, 26</sup>

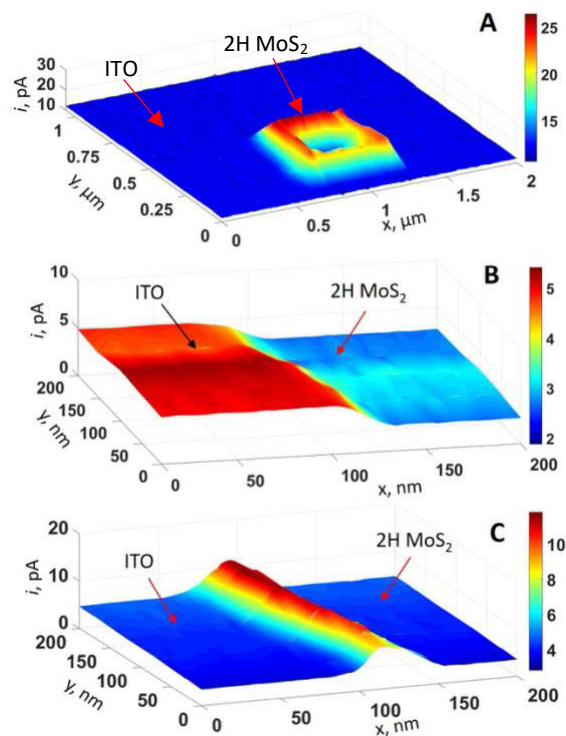


**Figure 2.** Imaging topography and HER activity of a pure 2H MoS<sub>2</sub> nanosheet on the ITO surface with SECM. (A) Submicrometer-scale SG/TC image of HER over a 2H MoS<sub>2</sub> flake. (B)

The high-resolution feedback mode image of the boundary between 2H MoS<sub>2</sub> and ITO as well as the corresponding (C) SG/TC mode (HER activity) images of a flake edge. See SI section for experimental conditions.

Figure 2A and 2C demonstrate that the HER rate of the basal 2H surface is immeasurably slow (i.e., essentially indiscernible from that of the catalytically inert ITO surface). Figure S2 shows a high-resolution feedback mode and SG/TC mode image of another 2H MoS<sub>2</sub> nanosheet, which has similar HER results. Our HER results qualitatively agree with the conclusions of Zhang et al. and Bentley et al.,<sup>22, 28</sup> with both studies finding higher reactivity for 2H MoS<sub>2</sub> edges relative to basal sites, although both of these prior studies have lower spatial resolution than realized in our study. Specifically, the experimental setup in Zhang et al. was unable to isolate edge and interior site reactivity, and the resolution in Bentley et al. was sub-micron, which would prohibit this SECCM experimental configuration from directly measuring the edges and basal sites of our MoS<sub>2</sub> nanosheets. Importantly, the <20 nm resolution achieved here *via* SECM enables us to conclusively and directly distinguish between edge and interior HER activity without relying upon indirect measurements for MoS<sub>2</sub> nanosheets.

The mixed-phase MoS<sub>2</sub> nanosheets are prepared by lithium-assisted exfoliation and deposited onto ITO (additional details are provided in the SI). XPS studies (Figure S3) taken at NREL one week after synthesis confirm that the nanosheets are mixed-phase, with both 2H (23%) and 1T (77%) phases co-existing within the population of nanosheets.<sup>20, 40</sup> Additional characterization of the mixed-phase MoS<sub>2</sub> nanosheets can be found in our recent publication.<sup>20</sup> SECM measurements show that the MoS<sub>2</sub> flakes (aged one to four weeks after delivery to CUNY-Queens) contain both the 2H and 1T phases *within one nanosheet*, which is consistent

with a recent report by Girish.<sup>41</sup> The activity maps of the mixed-phase MoS<sub>2</sub> nanosheets obtained with the Fc redox mediator (Figures 3A – 3C) point to the presence of the 1T phase. In a relatively low-resolution image of the mixed-phase nanosheet (Figure 3A), the 2H portion gives negative feedback ( $i_T \approx 13$  pA) while the 1T portion produces higher positive current feedback ( $i_T \approx 23$  pA) compared to the ITO substrate ( $i_T \approx 18$  pA). The 2D color map of the same area shows the 1T phase sandwiched by the 2H phase (Figure 3B). The conversion is not symmetric and appears to occur along straight lines. This conversion is likely caused by a sliding of the S plane and has a “ripple effect” along chemical bonds.<sup>42</sup> The zoomed-in map (Figure 3C) emphasizes the abruptness of the 1T-to-2H conversion boundary. In agreement with the approach curves in Figure S1A, unlike the 2H portion, positive feedback is measured across the entire 1T portion and not just the boundary. Note that the shipping and additional aging of the mixed-phase nanosheets for the SECM measurements may have increased the 2H:1T ratio compared to the ratio determined from XPS.

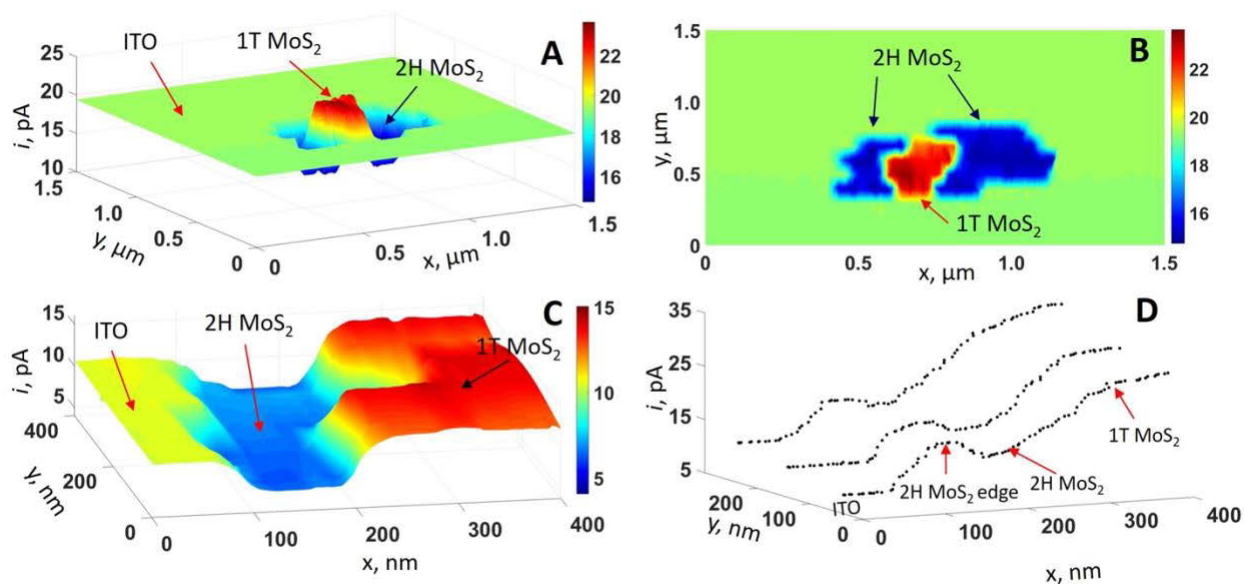


**Figure 3.** Imaging redox and HER activity of mixed-phase MoS<sub>2</sub> nanosheets. (A) Feedback mode image of a flake on ITO obtained with Fc redox mediator and (B) corresponding 2D color

map. (C) Zoom-in area showing a more detailed picture of boundaries between ITO, 2H MoS<sub>2</sub>, and 1T MoS<sub>2</sub> based on feedback current of Fc and (D) HER SG/TC line profiles across the same area of the substrate as in (C). See SI section for experimental conditions.

SG/TC mode is used to extract the line profiles (Figure 3D) to quantify the HER activity over the area of the mixed-phase MoS<sub>2</sub> nanoflake that is also imaged in the feedback mode (Figure 3C). By comparing these two figures, one can see that the 1T phase is very active for HER and that the 2H MoS<sub>2</sub> edges also exhibit significant activity toward HER. The tip current over the 2H interior is low but measurable, unlike the SG/TC images of the single-phase 2H MoS<sub>2</sub> flake (Figure 2C and S2B). This difference can likely be attributed to the large amount of H<sub>2</sub> generated at the 1T MoS<sub>2</sub> surface where diffusion can produce a broad concentration profile extending to the imaged 2H portion of the flake. This detailed information cannot be extracted from the lower resolution SG/TC image (Figure S4), which appears to suggest that the entire nanosheet is HER active, and the signal is dominated by the flux of hydrogen from the 1T phase.

Our SECM measurements suggest that the observed spatial differences in SECM current densities arise from spatial variation of 1T/2H phases within a nanosheet, but do not serve as a direct measurement of the spatial variation in atomic bonding environment. To address this issue, we turn to STEM and EELS measurements to confirm the phases within MoS<sub>2</sub> nanosheets. Taking advantage of the high-spatial resolution of STEM and high-energy resolution of EELS, we identify the electron energy difference of sulfur at a MoS<sub>2</sub> nanosheet edge and center. Figure 4A shows the STEM-bright field (STEM-BF) image for an individual MoS<sub>2</sub> flake that has been aged for three weeks to foster the partial transition from 1T to 2H. The contrast varies across the nanosheet, indicating possible defects and thickness differences across the flake.<sup>43, 44</sup> The

normalized EELS spectra of the S-L<sub>2,3</sub> edge at two spots (indicated in Figure 4A) are displayed in Figure 4B, where the lower energy feature (~161 – 164 eV, S 2p<sub>3/2</sub> + S 2p<sub>1/2</sub> states → S 3p) is the pre-edge and the higher energy feature (~ 170 – 176 eV, S 2p<sub>3/2</sub> + S 2p<sub>1/2</sub> states → S 4d) is the primary edge.<sup>45</sup> The S-L<sub>2,3</sub> transition is ~2 eV higher energy at the nanosheet edge than in the center. These results are consistent with the edge being the 2H phase and the interior being the 1T phase, an interpretation supported by XPS data (Figure S3), which show the S 2p binding energy shifts to higher energy upon converting from 1T to 2H.

Further support for this phase assignment stems from different electron exposure times for the EELS measurements. The center of the MoS<sub>2</sub> EELS data does not change as a function of electron exposure time, whereas the S-L<sub>2,3</sub> edge shifts to lower energy following longer exposures (Figure S5). Several studies have demonstrated that the electron beam used in STEM measurements can supply enough electrons to induce the 2H to 1T phase transition.<sup>46-48</sup> Thus, the shift to lower energy observed in Figure S5 is consistent with conversion from the 2H to 1T phase due to excess negative charge supplied by the electron beam. The EELS results on mixed-phase MoS<sub>2</sub> nanosheets are thus consistent with our SECM data, suggesting that the 1T phase is surrounded by the 2H phase.

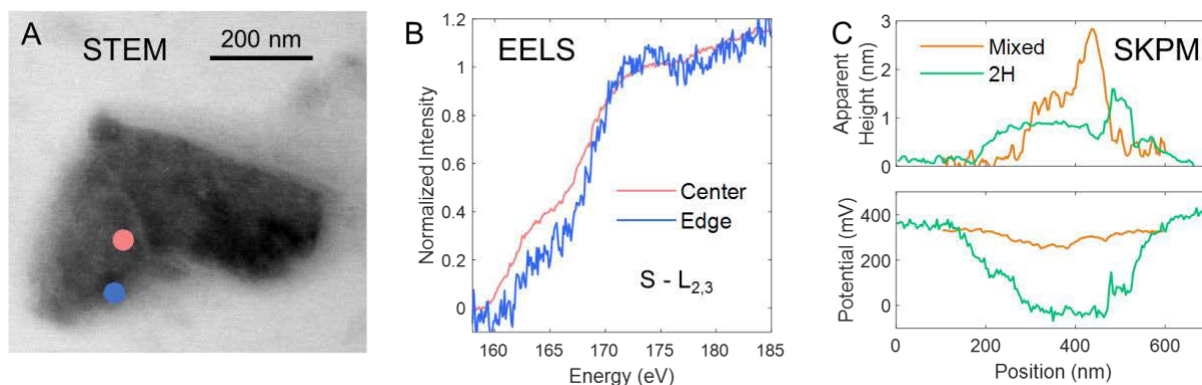


**Figure 4.** Nanoscale characterization of MoS<sub>2</sub> nanosheets. (A) STEM-BF image of an individual mixed-phase MoS<sub>2</sub> nanosheet. (B) EELS spectra of the mixed-phase MoS<sub>2</sub> nanosheet at the edge (blue dot in Figure 4A) and center (red dot in Figure 4A). Intensities are normalized to the average between 170 – 180 eV. (C) SKPM measurements were taken before and after conversion to 2H-only phase, where the MoS<sub>2</sub> nanosheets were deposited on a highly-conducting silicon substrate. Figure shows apparent height profiles (top) and corresponding surface potential profiles (bottom) of representative mixed-phase and 2H-only MoS<sub>2</sub> nanosheets (not same nanosheet, images in Figure S6).

Finally, we aim to corroborate our SECM measurements by evaluating the local phase changes across MoS<sub>2</sub> nanosheets using scanning Kelvin probe microscopy (SKPM), which measures local surface potential variations. We expect to measure a surface potential difference between the two phases, which is directly related to the local workfunction and, therefore, its reactivity towards HER. Details of the SKPM methodology and analysis are included in the SI. We examine the SKPM of mixed-phase MoS<sub>2</sub> (aged two weeks and stored at room temperature/refridgeration to prevent conversion to 2H) and thermally annealed MoS<sub>2</sub> (2H-only) on a highly-conducting Si substrate – imaging both surface morphology (apparent height) and the surface potential simultaneously.<sup>49-51</sup> The MoS<sub>2</sub> nanosheets are 1 – 3 nm tall and 200 – 400 nm wide (Figure 4C (top) and Figure S6). For each apparent height profile over mixed-phase and 2H-only MoS<sub>2</sub>, the corresponding surface potential profiles are shown (Figure 4C (bottom) and Figure S6).

For the mixed-phase MoS<sub>2</sub>, we measure  $\sim +250 (\pm 50)$  mV surface potential difference between the probe tip and the mixed-phase MoS<sub>2</sub>; for the 2H-only MoS<sub>2</sub>, we measure  $\sim +50$

( $\pm 50$ ) mV. This change in surface potential difference corresponds to the mixed phase MoS<sub>2</sub> possessing a shallower workfunction (i.e., the Fermi level is closer to the vacuum level) compared to 2H-only MoS<sub>2</sub>. Since HER activity is related to the chemical potential of electrons in the MoS<sub>2</sub> nanosheets, the measured differences in local workfunction observed for mixed-phase and 2H-only nanosheets is consistent with the improved HER activity observed in SECM for the mixed-phase MoS<sub>2</sub>. In our SKPM images of the mixed-phase MoS<sub>2</sub>, we do not observe spatially-varying surface potential changes across individual nanosheets, possibly due to a combination of the smaller amount of the 2H phase combined with the averaging effect from the tip size.

## Conclusions

In conclusion, we use high-resolution SECM to map the HER activity of solution-exfoliated MoS<sub>2</sub> nanosheets on ITO. Fully converted 2H MoS<sub>2</sub> nanosheets have edges that are active for HER and Fc<sup>+</sup> reduction, while the interior is essentially inactive for HER. High spatial resolution (<20 nm) is essential for correctly discerning between the edge and basal areas in 2H MoS<sub>2</sub>. Furthermore, we show that (before annealing or time-dependent conversion fully back to 2H) solution-exfoliated MoS<sub>2</sub> nanosheet populations are not composed of nanosheets that are fully in either the 1T or 2H phase but instead are mixed-phase within the nanosheets. In this SECM measurement on mixed phase MoS<sub>2</sub> nanosheet, conversion appears to proceed from the outside of a nanosheet inwards and along straight lines, which is likely due to the sliding of the S plane. By combining high-resolution SECM data with XPS, STEM-EELS, and SKPM, we gained additional insight about the mixed-phase MoS<sub>2</sub>, such as the mixed phase has a shallower local workfunction compared to the 2H MoS<sub>2</sub>, which could change the thermodynamic driving

force for H<sub>2</sub> generation. This study highlights the importance of fully converting the 2H MoS<sub>2</sub> phase into the 1T phase and stabilizing this phase for increased HER activity.

### **Supporting Information**

The Supporting Information contains the Experimental Section for sample preparation and characterization. There are additional figures for the feedback mode SECM responses, 2D SECM color maps of the topography and reactivity of 2H MoS<sub>2</sub> nanosheets, XPS of the mixed-phase and 2H MoS<sub>2</sub> nanosheets, low-resolution SG/TC map of HER on mixed-phase MoS<sub>2</sub> nanosheets, STEM-EELS spectra of mixed MoS<sub>2</sub> nanosheets, and SKPM of mixed-phase and 2H MoS<sub>2</sub> nanosheets.

### **Conflicts of Interest**

There are no conflicts to declare.

### **Acknowledgements**

The support of the SECM work by the National Science Foundation (CHE-1416116; MVM) is gratefully acknowledged. The MoS<sub>2</sub> exfoliation, XPS, SKPM, and STEM-EELS work was authored by Alliance for Sustainable Energy, LLC, the manager and operator of the National Renewable Energy Laboratory for the U.S. Department of Energy under Contract No. DE-AC36-08GO28308. Funding provided by U.S Department of Energy, Office of Science, Office of Basic Energy Sciences, Division of Chemical Sciences, Geosciences and Biosciences. The views expressed in the article do not necessarily represent the views of the Department of Energy or the U.S. Government. The U.S. Government retains and the publisher, by accepting the article for

publication, acknowledges that the U.S. Government retains a nonexclusive, paid-up, irrevocable, worldwide license to publish or reproduce the published form of this work, or allow others to do so, for U.S. Government purposes.

## References

1. G. W. Crabtree, M. S. Dresselhaus and M. V. Buchanan, *Phys Today*, 2004, **57**, 39-44.
2. *Platinum Quarterly Q2 2017*, World Platinum Investment Council, 2017.
3. M. A. Lukowski, A. S. Daniel, C. R. English, F. Meng, A. Forticaux, R. J. Hamers and S. Jin, *Energy & Environmental Science*, 2014, **7**, 2608-2613.
4. Y. Yin, Y. Zhang, T. Gao, T. Yao, X. Zhang, J. Han, X. Wang, Z. Zhang, P. Xu, P. Zhang, X. Cao, B. Song and S. Jin, *Adv. Mater.*, 2017, **29**, 1700311.
5. Q. Ding, B. Song, P. Xu and S. Jin, *Chem*, 2016, **1**, 699-726.
6. D. A. Henckel, O. M. Lenz, K. M. Krishnan and B. M. Cossairt, *Nano Lett.*, 2018, **18**, 2329-2335.
7. X. Duan, J. Xu, Z. Wei, J. Ma, S. Guo, H. Liu and S. Dou, *Small Methods*, 2017, **1**, 1700156.
8. H. Li, X. Jia, Q. Zhang and X. Wang, *Chem*, 2018, **4**, 1510-1537.
9. A. Ambrosi, Z. Sofer and M. Pumera, *Small*, 2015, **11**, 605-612.
10. J. Cui, R. Jiang, W. Lu, S. Xu and L. Wang, *Small*, 2017, **13**, 1602235-1602235.
11. Y. Kang, Y. Gong, Z. Hu, Z. Li, Z. Qiu, X. Zhu, P. M. Ajayan and Z. Fang, *Nanoscale*, 2015, **7**, 4482-4488.
12. J. H. Lee, W. S. Jang, S. W. Han and H. K. Baik, *Langmuir*, 2014, **30**, 9866-9873.
13. Y. Lei, S. Pakhira, K. Fujisawa, X. Wang, O. O. Iyiola, N. Perea López, A. Laura Elías, L. Pulickal Rajukumar, C. Zhou, B. Kabius, N. Alem, M. Endo, R. Lv, J. L. Mendoza-Cortes and M. Terrones, *ACS Nano*, 2017, **11**, 5103-5112.
14. H. Li, C. Tsai, A. L. Koh, L. Cai, A. W. Contryman, A. H. Fragapane, J. Zhao, H. S. Han, H. C. Manoharan, F. Abild-Pedersen, J. K. Nørskov and X. Zheng, *Nat. Mater.*, 2016, **15**, 48-53.
15. Q. Liu, Q. Fang, W. Chu, Y. Wan, X. Li, W. Xu, M. Habib, S. Tao, Y. Zhou, D. Liu, T. Xiang, A. Khalil, X. Wu, M. Chhowalla, P. M. Ajayan and L. Song, *Chem. Mater.*, 2017, **29**, 4738-4744.
16. M. A. Lukowski, A. S. Daniel, F. Meng, A. Forticaux, L. Li and S. Jin, *J. Am. Chem. Soc.*, 2013, **135**, 10274-10277.
17. Y. Shi, J. Wang, C. Wang, T.-T. Zhai, W.-J. Bao, J.-J. Xu, X.-H. Xia and H.-Y. Chen, *J. Am. Chem. Soc.*, 2015, **137**, 7365-7370.
18. D. Voiry, M. Salehi, R. Silva, T. Fujita, M. Chen, T. Asefa, V. B. Shenoy, G. Eda and M. Chhowalla, *Nano Lett.*, 2013, **13**, 6222-6227.
19. Y. Yin, J. Han, Y. Zhang, X. Zhang, P. Xu, Q. Yuan, L. Samad, X. Wang, Y. Wang, Z. Zhang, P. Zhang, X. Cao, B. Song and S. Jin, *J. Am. Chem. Soc.*, 2016, **138**, 7965-7972.
20. E. E. Benson, H. Zhang, S. A. Schuman, S. U. Nanayakkara, N. D. Bronstein, S. Ferrere, J. L. Blackburn and E. M. Miller, *J. Am. Chem. Soc.*, 2018, **140**, 441-450.

21. T. F. Jaramillo, K. P. Jørgensen, J. Bonde, J. H. Nielsen, S. Horch and I. Chorkendorff, *Science*, 2007, **317**, 100-102.
22. J. Zhang, J. Wu, H. Guo, W. Chen, J. Yuan, U. Martinez, G. Gupta, A. Mohite, M. Ajayan Pulickel and J. Lou, *Adv. Mater.*, 2017, **29**, 1701955.
23. I. H. Kwak, I. S. Kwon, H. G. Abbas, G. Jung, Y. Lee, J. Park and H. S. Kang, *J. Mater. Chem. A*, 2018, **6**, 5613-5617.
24. U. Maitra, U. Gupta, M. De, R. Datta, A. Govindaraj and C. N. R. Rao, *Angew. Chem. Int. Ed.*, 2013, **52**, 13057-13061.
25. J. Rodriguez-Lopez, C. G. Zoski and A. J. Bard, in *Scanning Electrochemical Microscopy*, eds. A. J. Bard and M. V. Mirkin, CRC Press, 2nd edn., 2012, ch. 16, pp. 525-568
26. T. Sun, D. Wang, M. V. Mirkin, H. Cheng, J.-C. Zheng, R. M. Richards, F. Lin and H. L. Xin, *Nat. Nanotechnol.*, 2018, **submitted**.
27. M. Kang, D. Perry, C. L. Bentley, G. West, A. Page and P. R. Unwin, *ACS Nano*, 2017, **11**, 9525-9535.
28. C. L. Bentley, M. Kang, F. M. Maddar, F. Li, M. Walker, J. Zhang and P. R. Unwin, *Chem. Sci.*, 2017, **8**, 6583-6593.
29. X. Feng, K. Jiang, S. Fan and M. W. Kanan, *J. Am. Chem. Soc.*, 2015, **137**, 4606-4609.
30. C. L. Bentley, C. Andronescu, M. Smialkowski, M. Kang, T. Tarnev, B. Marler, P. R. Unwin, U.-P. Apfel and W. Schuhmann, *Angew. Chem. Int. Ed.*, 2018, **57**, 4093-4097.
31. R. G. Mariano, K. McKelvey, H. S. White and M. W. Kanan, *Science*, 2017, **358**, 1187-1192.
32. J. H. K. Pfisterer, Y. Liang, O. Schneider and A. S. Bandarenka, *Nature*, 2017, **549**, 74.
33. H. Li, M. Du, M. J. Mleczko, A. L. Koh, Y. Nishi, E. Pop, A. J. Bard and X. Zheng, *J. Am. Chem. Soc.*, 2016, **138**, 5123-5129.
34. D. V. Esposito, I. Levin, T. P. Moffat and A. A. Talin, *Nat. Mater.*, 2013, **12**, 562.
35. J. Kim, C. Renault, N. Nioradze, N. Arroyo-Currás, K. C. Leonard and A. J. Bard, *J. Am. Chem. Soc.*, 2016, **138**, 8560-8568.
36. J. Rodríguez-López, N. L. Ritzert, J. A. Mann, C. Tan, W. R. Dichtel and H. D. Abruña, *J. Am. Chem. Soc.*, 2012, **134**, 6224-6236.
37. T. Sun, Y. Yu, B. Zacher, J. and M. V. Mirkin, *Angew. Chem. Int. Ed.*, 2014, **53**, 14120-14123.
38. C. Tan, J. Rodríguez-López, J. J. Parks, N. L. Ritzert, D. C. Ralph and H. D. Abruña, *ACS Nano*, 2012, **6**, 3070-3079.
39. S. Amemiya, in *Electroanalytical Chemistry: A Series of Advances*, eds. A. J. Bard and C. G. Zoski, CRC press, 2015, vol. 26, pp. 1-72.
40. K. C. Knirsch, N. C. Berner, H. C. Nerl, C. S. Cucinotta, Z. Gholamvand, N. McEvoy, Z. Wang, I. Abramovic, P. Vecera, M. Halik, S. Sanvito, G. S. Duesberg, V. Nicolosi, F. Hauke, A. Hirsch, J. N. Coleman and C. Backes, *ACS Nano*, 2015, **9**, 6018-6030.
41. Y. R. Girish, R. Biswas and M. De, *Chem. Eur. J.*, 2018, **24**, 13871-13878.
42. X. Gan, L. Y. S. Lee, K.-y. Wong, T. W. Lo, K. H. Ho, D. Y. Lei and H. Zhao, *ACS Appl. Energy Mater.*, 2018, **1**, 4754-4765.
43. H. C. Nerl, K. T. Winther, F. S. Hage, K. S. Thygesen, L. Houben, C. Backes, J. N. Coleman, Q. M. Ramasse and V. Nicolosi, *NPJ 2D Mater. Appl.*, 2017, **1**, 2.

44. H. E. K. E. MacArthur, T. J. Pennycook, E. Okunishi, A. J. D'Alfonso, N. R. Lugg, L. J. Allen and P. D. Nellist, *Ultramicroscopy*, 2013, **133**, 109-119.
45. A. Parija, Y.-H. Choi, Z. Liu, J. L. Andrews, L. R. De Jesus, S. C. Fakra, M. Al-Hashimi, J. D. Batteas, D. Prendergast and S. Banerjee, *ACS Cent. Sci.*, 2018, **4**, 493-503.
46. K.-L. Tai, G.-M. Huang, C.-W. Huang, T.-C. Tsai, S.-K. Lee, T.-Y. Lin, Y.-C. Lo and W.-W. Wu, *Chem. Commun.*, 2018, **54**, 9941-9944.
47. Y.-C. Lin, D. O. Dumcenco, Y.-S. Huang and K. Suenaga, *Nat. Nanotechnol.*, 2014, **9**, 391-396.
48. M. R. Ryzhikov, V. A. Slepko, S. G. Kozlova, S. P. Gabuda and V. E. Fedorov, *J. Comput. Chem.*, 2015, **36**, 2131-2134.
49. S. U. Nanayakkara, G. Cohen, C.-S. Jiang, M. J. Romero, K. Maturova, M. Al-Jassim, J. van de Lagemaat, Y. Rosenwaks and J. M. Luther, *Nano Lett.*, 2013, **13**, 1278-1284.
50. S. U. Nanayakkara, J. van de Lagemaat and J. M. Luther, *Chem. Rev.*, 2015, **115**, 8157-8181.
51. C.-S. Jiang, M. Yang, Y. Zhou, B. To, S. U. Nanayakkara, J. M. Luther, W. Zhou, J. J. Berry, J. van de Lagemaat, N. P. Padture, K. Zhu and M. M. Al-Jassim, *Nature Communications*, 2015, **6**, 8397.